

# **On the relationships between depth migration of marine controlled-source electromagnetic and seismic data**

KETIL HOKSTAD and TAGE RØSTEN, Statoil Research Centre, Trondheim, Norway

Remote sensing techniques record variations in subsurface petrophysical parameters, such as seismic, electromagnetic, and potential-field properties. Seismic is by far the most common technique, using acoustic and elastic waves to map boundaries between buried strata with contrasting pressure (P) and shear (S) wave velocities. High-resolution data provide information about geologic structures and potential hydrocarbon traps and sometimes allow inferences to be made about the composition of reservoir pore fluids (oil, gas, brine, or combinations) and their relative saturations. Nevertheless, hydrocarbon-filled sandstone reservoirs are often better detected by electrical resistivity rather than seismic parameters (e.g., P-wave velocities are less affected by variations in brine saturation than electrical resistivity).

Statoil has pioneered and developed a marine controlled-source electromagnetic (MCSEM) method—sometimes called seabed logging (SBL)—to remotely identify relatively thin, high-resistivity intervals in areas with water depths typically greater than 200–300 m. The principle is that oil and gas are highly resistive compared with brine-filled sandstones. SBL surveys have already given promising results when used as a complement to seismic. However, the method is not foolproof because several rock types—such as salt and igneous intrusives—also are highly resistive.

CSEM uses a horizontal electric dipole that emits a low-frequency electromagnetic signal into the underlying seabed and downward. As the upper sediments are effectively partial conductors, the penetration of EM fields is limited by the skin depth. In practice this means that the technique requires a low-frequency EM source, normally 0.1–5 Hz (cf., 3–100 Hz for seismic) for about 2000–3000 m subsurface penetration. EM energy is constantly refracted back to the surface where it is detected by EM receivers deployed on the seabed. When the source-receiver distance (offset) is larger than the reservoir burial depth, energy from the resistive interval directly dominates the transmitted energy. The detection of “guided and refracted” energy is the basis of the method.

CSEM technology—for both marine and land—clearly has considerable potential for hydrocarbon exploration. We expect to see significant advances arising from sophisticated 3D acquisition, imaging, and inversion of all EM effects constrained by seismic and potential field data (magnetometry and gravimetry). As it further matures, CSEM may well prove to be the most important method for probing the subsurface since the emergence of 3D seismic surveying more than 25 years ago. However, as stated above, it is not a “silver bullet” and must be carefully combined with complementary data to reveal ambiguities and avoid misinterpretation.

This paper describes the relationships between imaging or depth migration of seismic and frequency-domain CSEM data. We explain the principles of imaging and focus on the similarities and dissimilarities between seismic and CSEM depth migration. Although we restrict the discussion and examples to the marine case, the theory and methodology are applicable to land CSEM methods including transient EM sources. We give an example of field SBL data by considering 3D explicit finite-difference depth migration using one-way wavefield operators.

**Table 1.** Comparison of important data acquisition and wavefield recording characteristics between seismic data and frequency domain CSEM.

	Seismic	CSEM
Number of frequencies	>> 100	<10
Shot (Tx) spacing	~50 m	~100 m
Receiver (Rx) spacing	~50 m	~1000 m
Type of measurement	far field	near field
Green's functions	2D/3D almost equal	2D/3D very different
2D data	2D imaging schemes	3D imaging schemes
3D data	3D imaging schemes	3D imaging schemes

**Background.** In relatively unexplored areas, geoscientists have to rely largely on geologic inferences made from geo-physical data to identify and evaluate potential hydrocarbon prospects. Traditionally, this has been based on acoustic (seismic) interpretation to delineate structures, potential reservoir rock volumes and, occasionally, fluid contacts. What was missing, however, was a better way of gaining information on fluid contents prior to drilling. This is where the CSEM-SBL method, invented and commercialized by Statoil, comes to the fore. The principle is based on the contrasting resistivities between oil/gas (high resistivity) and saline formation water (low resistivity) which can be detected by measuring the subsurface response to ultralow-frequency electromagnetic, diffusive wavefields.

A subsurface resistivity anomaly is not a unique hydrocarbon indicator. It may be related to other resistive bodies or layers in the subsurface, such as salt and igneous intrusions (sills) or regional trends (e.g., basin thickening). EM depth-migration schemes are useful in upgrading and visualizing MCSEM data in three dimensions. The nature of CSEM data includes several advantages that make it possible to run full 3D depth migration three orders of magnitude faster compared to seismic data. This permits extremely rapid testing and evaluation of different real-size 3D models through repeated depth migration. The results can then be used to obtain improved initial models for full 3D inversion schemes, thereby reducing the number of iterations as well as computer costs.

Zhdanov et al. (1996) introduced depth migration for CSEM data, based on Gazdag's frequency-wavenumber ( $f$ - $k$ ) migration and Claerbout's  $45^\circ$  finite-difference (FD) equation (Claerbout, 1985). Tompkins (2004) presented work about 2D isotropic frequency-domain CSEM imaging. Mittet et al. (2005) developed a 3D depth-migration algorithm using an approach very related to reverse-time migration. Hokstad and Røsten (2006) presented 2D  $f$ - $k$  and FD anisotropic depth-migration schemes. Røsten et al. (2006) developed schemes for 3D  $f$ - $k$  depth migration and explicit 3D FD depth migration of CSEM data, by following the approach of Gazdag (1978) and Holberg (1988) for 2D  $f$ - $k$  and FD seismic depth-migration schemes, respectively. The

3D FD approach will be used as an example in this paper.

This novel 3D EM migration code was developed by modification of an existing seismic depth-migration code—originally developed for 3D ocean-bottom seismic data—running in parallel under the message passing interface (MPI) on massive Linux clusters. This allowed very rapid implementation of the EM migration scheme, because only minor modifications of the code were required.

Now we explain the relationships between depth migration of seismic and CSEM data in more detail.

**Relationships.** If the background medium is sufficiently smooth, the propagation properties of both seismic and EM wavefields can be represented in the frequency-space ( $f$ - $x$ ) domain by Helmholtz-type differential equations (e.g., Løseth et al., 2006). Consequently, similar migration schemes can be applied to both types of data. Most  $f$ - $x$  domain migration schemes developed for seismic imaging can easily be adapted for depth migration of CSEM data. In isotropic background media, the dispersion relations of seismic and EM fields are formally equal.

There are, however, important details that are different and must be accounted for. We will split the following discussion into these subsections: (1) data acquisition and wavefield recording; (2) preprocessing; (3) one-way equations; (4) wavefield extrapolation; (5) digital filter design for explicit finite-difference operators; and (6) imaging condition.

*Data acquisition and wavefield recording.* Table 1 summarizes the main differences between acquisition geometries and important wavefield recording issues. The first three rows compare the typical dimensions between seismic data and frequency-domain CSEM. Frequency-domain CSEM has a discontinuous frequency spectrum. Usually, the fundamental frequency and a few (odd) harmonics can be used in the imaging. The number of discrete frequency components is typically less than 10, and commonly not more than 5–7, approximately covering the range from 0.1 to 5 Hz. Seismic data have, on the other hand, a dense (and in principle continuous) frequency spectrum, and the number of discrete frequencies—covering the unaliased frequency range from 3 to 100 Hz—is several hundred. After binning, the shot sampling for CSEM is typically 50 or 100 m while the shot spacing for seismic data is often 25 or 50 m. On the receiver side, CSEM is much more sparsely sampled than seismic data (i.e., around 500–1000 m compared to 25–100 m for seismic). From the size of data point of view, and by only considering 2D data acquisition, frequency-domain CSEM depth migration will run about three orders of magnitude faster than for imaging of seismic data. The speed will be about four times faster for full 3D acquisition.

Another issue of major importance is the difference in phase properties of 2D and 3D field extrapolators (Green's functions). CSEM data are often acquired with 2D line geometries. However, in the imaging it is important to account for the 3D nature of the EM fields. Otherwise, target conductivity anomalies may image at the wrong depth. Seismic data are recorded in the far field, where the 2D phase is an excellent approximation to the 3D phase of the field data. Hence, seismic 2D lines can be migrated using 2D migration schemes. For CSEM data, near-field effects can be important, and the phase of 2D and 3D field extrapolators differ significantly.

*Preprocessing.* The preprocessing steps of CSEM and seismic data prior to depth migration are in principle the same. For frequency-domain imaging, both types of data are transformed to the frequency-domain and binned into discrete sets of data points in space. CSEM data are typically orga-

nized in common-receiver gathers. Ocean-bottom seismic data are also commonly organized into common-receiver gathers; for streamer seismic data, both common-shot and common-receiver data are used. In preprocessing prior to one-way equation-based migration, the upgoing scattered field due to the resistivity anomalies should be separated from the total field, which also includes the direct wave and the “air wave” generated at the sea surface (Amundsen et al., 2006). Typical preprocessing steps include: (1) correction for source and receiver orientation; (2) Fourier transform from time to frequency; (3) normalization with respect to source and receiver dipole moments; (4) calibration of source and receiver impulse responses; and (5) separation of down-going (incident) and upgoing (scattered) wavefields. The latter is a prerequisite for depth-stepping migration methods. It can more generally be seen as a free-surface-related multiple attenuation step that is necessary to image the primaries correctly—i.e., designature and demultiple by calculating  $U/D$  (Amundsen, 2005).

*One-way equations.* In the ultralow-frequency approximation, the Maxwell equations in the frequency domain can be written as

$$\begin{aligned}\nabla \times \mathbf{E} &= i\omega\mu_0 \mathbf{H} \\ \nabla \times \mathbf{H} &= \mathbf{J}\end{aligned}\quad (1)$$

where  $\mathbf{E}$  is the electric field,  $\mathbf{H}$  is the magnetic field,  $\mu_0$  is the vacuum permeability, and  $\omega$  is the angular frequency. We assume a linear medium, zero source current density, and that the conduction current density  $\mathbf{J}$  is given by Ohm's law

$$\mathbf{J} = \sigma \mathbf{E} \quad (2)$$

where  $\sigma$  is the isotropic conductivity. Combining the above equations to eliminate the magnetic field, and assuming a charge-free medium such that  $\nabla \cdot \mathbf{E} = 0$  (valid for an isotropic and smooth model), we obtain the Helmholtz equation

$$\nabla^2 E_i + \kappa_0^2 E_i = 0 \quad (3)$$

for each component  $E_i$  of the electric field. The same equation is the basis for seismic compressional-wave (P-wave) migration.

In seismic depth migration, compensation for absorption and attenuation is feasible (Mittet et al., 1995), but is rarely applied. Hence, in most seismic depth migration methods, the wavenumber  $k$  is real and depends linearly on frequency

$$k = \omega / c \quad (4)$$

with  $c$  being the seismic (P-wave) velocity. Low-frequency EM fields are governed by a diffusive wave equation. The EM wavenumber  $\kappa_0$  is complex and proportional to the square-root of the frequency

$$\kappa_0 = \sqrt{i\omega\mu_0\sigma} \quad (5)$$

Both the propagation and attenuation of low-frequency EM fields are controlled by a single physical parameter, the conductivity (a tensor in anisotropic media). Consequently, attenuation cannot be neglected. The adjoint Helmholtz equation is obtained by changing the sign of the last term in Equation 3.

Assuming a 1D background medium, and Fourier transforming over the horizontal spatial coordinates, Equation 3 readily leads to one-way equations in the  $f$ - $k$ -domain for downgoing (incident) fields  $E_i^D$  and upgoing (scattered)

fields  $E_i^U$ . From the adjoint Helmholtz equation, we correspondingly obtain a one-way equation for the so-called migrated field  $E_i^M$ , introduced by Zhdanov et al. (1996). The migrated field is equal to the upgoing field at the recording surface but differs elsewhere. The one-way equations for the electric field in the  $f\text{-}k$  domain can be written:

$$\partial_z E_i^v = \gamma k_z E_i^v \quad (6)$$

where

$$k_z = \sqrt{\kappa_0^2 + \gamma^2 (k_x^2 + k_y^2)} \quad (7)$$

is the vertical wavenumber, and  $\gamma = i$  for  $v = D$  (downgoing wavefields),  $\gamma = -i$  for  $v = U$  (upgoing wavefields) and  $\gamma = -1$  for  $v = M$  (migrated wavefields). The sign convention in the Fourier transform is such that  $\partial_t \leftrightarrow -i\omega$  and  $\partial_i \leftrightarrow ik_i$ . The solution to Equation 6 is:

$$E_i''(k_x, k_y, z + \Delta z, \omega) = \exp(\gamma \Delta z k_z) E_i^v(k_x, k_y, z, \omega) \quad (8)$$

which is the basis for the wavefield extrapolation step of (Gazdag)  $f\text{-}k$  based depth migration. The depth-stepping equation for  $E_i^D$  decays exponentially and is numerically stable. The equation for  $E_i^U$  grows exponentially and is numerically unstable. It can, however, be applied in a "phase-only" migration scheme, if only the real part of the vertical wavenumber  $k_z$  is used in the downward continuation. The depth-stepping equation for  $E_i^M$  is numerically stable with exponential decay (like  $E_i^D$ ) and backward phase rotation (like  $E_i^U$ ). The  $f\text{-}k$  migration operators are accurate up to 90° from the vertical, but limited to 1D background media.

The one-way equation for seismic data will be likewise. The only difference is the phase-shift operator  $\exp(\gamma \Delta z k_z)$  due to a different dispersion relation.

*Digital filter design for explicit finite-difference operators.* The problem with direct application of Equation 8 is that the simple multiplication in the  $f\text{-}k$  domain rules out the possibility of applying laterally varying resistivity (or velocity) model. To relax the 1D background assumption, we replace the phase-shift operator in Equation 8 by discrete convolution filters  $W^v(m\Delta x, n\Delta y, \hat{k}_0)$  in the  $f\text{-}x$  domain, as proposed by Holberg (1988). Then the extrapolation of the electric field can be written:

$$E_i'(x, y, z + \Delta z, \omega) = \sum_{m,n=-L}^L [W^v(m\Delta x, n\Delta y, \hat{k}_0) \times E_i^v(x - m\Delta x, y - n\Delta y, z, \omega)] \quad (9)$$

The convolution operators depend only on the normalized wavenumber  $\hat{k}_0 = \kappa_0 \Delta x$  (assuming that  $\Delta x = \Delta y$ ) and the ratio  $\hat{k}_0 / \Delta x$ . Hence, for a given  $\Delta z / \Delta x$  ratio, the operator coefficients can be precomputed for all relevant values of  $\hat{k}_0$  and stored in a table. For simplicity we assume in the examples that  $\Delta y = \Delta x$  and  $\Delta z / \Delta x = 0.5$ . Computation of the finite impulse-response filter with complex-valued coefficients  $W^v(m\Delta x, n\Delta y, \hat{k}_0)$ , is posed as an inverse problem, minimizing the objective function in the  $L_4$ -norm

$$J = \|W^v(i\Delta k_x, j\Delta k_y, \hat{k}_0) - \exp(\gamma \Delta z k_z)\|^4 \quad (10)$$

where  $W^v(i\Delta k_x, j\Delta k_y, \hat{k}_0)$  is the discrete Fourier transform of  $W^v(m\Delta x, n\Delta y, \hat{k}_0)$  for a discrete set of horizontal wavenumbers  $i\Delta k_x$  and  $j\Delta k_y$ .

The seismic dispersion relation is discontinuous at the transition to the evanescent region where  $k_z = 0$ , see Figure 1a. Hence, the filter operators for seismic 3D depth migration are only matched to propagating waves by introduc-

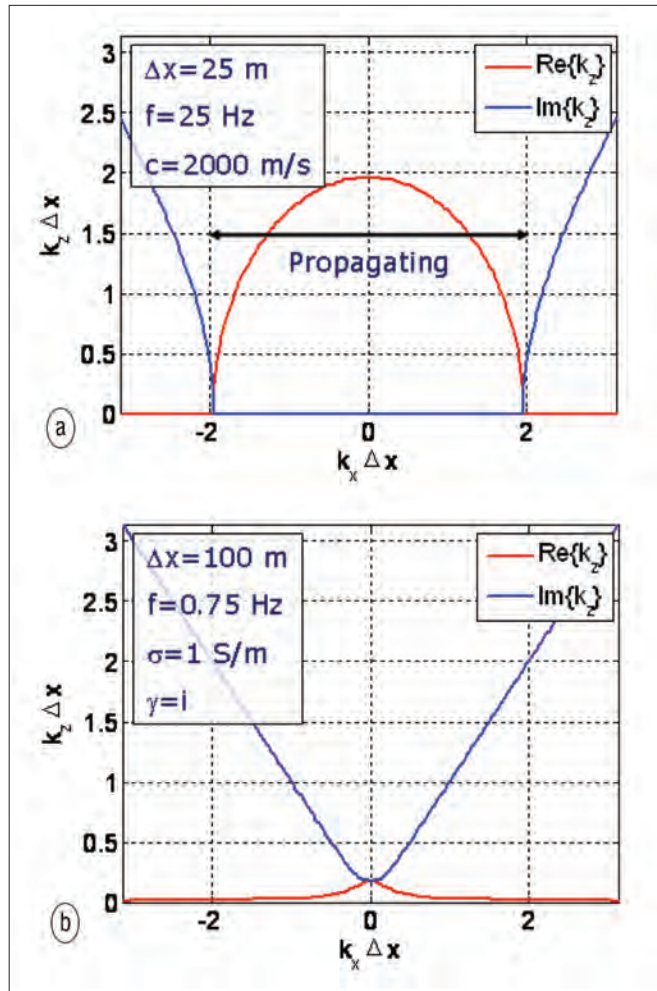


Figure 1. Vertical wavenumbers for (a) seismic data and (b) CSEM data. For the seismic case we neglect dispersion and absorption and assume  $\Delta x = 25$  m,  $f = 25$  Hz, and  $c = 2000$  m/s. For the CSEM case we assume  $\Delta x = 100$  m, and  $f = 0.25$  Hz and  $\sigma = 1$  S/m.  $\gamma = i$  (i.e., downgoing wavefields).

ing a dip-limitation. The evanescent waves are damped to get a stable explicit 3D depth migration scheme. The real and imaginary parts of the dispersion relation for diffusive EM fields are smooth and continuous for all wavenumbers, see Figure 1b. Hence, we do not need to introduce a dip-limitation on the corresponding 3D filter operators to get a stable depth migration scheme for CSEM data. The optimization is generally performed for all wavenumbers, and the real and imaginary part of the filter operator are optimized separately. In practice, we need to compute tabulated filter coefficients only for  $W^D$ . Then the operator for  $W^M$  can be obtained by complex conjugation. Table 2 summarizes some important differences between 3D explicit digital filter operator design of seismic data and CSEM.

We use basically the same layout of the explicit 3D digital filter coefficients as proposed by Mittet (2006) for seismic data (Figure 2). Blacquiere et al. (1989) used several symmetries of the full 3D extrapolation operator. In Mittet's approach, the filter coefficients of the central part of the full 3D operator remain unaltered with respect to Blacquiere, whereas the outer extrapolation coefficients are constrained to be equal as a function of operator radius. This reduces the number of floating-point operations required to do depth extrapolation because the number of complex multiplications are replaced by complex additions. In addition, Mittet's approach has negligible numerical induced anisotropy due

to the highly symmetrical frequency responses offered by the outer extrapolation coefficients. Mittet used as an example a core-area filter half-length equal to  $L = 6$  and total-area filter half-length equal to  $M = 12$ . For CSEM data, we use a core-area filter half-length equal to  $L = 8$  and total-area filter half-length equal to  $M = 11$ . The numerical cost for Mittet's layout example is about 1200 floating point numbers per grid point per frequency, and is about 1100 for the layout shown in Figure 2.

Figure 3 shows the magnitude and phase responses for  $\exp(i\Delta z k_z)$  (i.e., downgoing operator) assuming ( $\sigma = 1.0 \text{ S/m}$  and  $f = 0.75 \text{ Hz}$ ). Figure 4 shows the corresponding magnitude and phase responses for the optimized 3D spatial digital filters. In the filter design the number of discrete positive horizontal wavenumbers are  $I = J = 64$ . Note the excellent match for both the magnitude and the phase.

*Wavefield extrapolation.* Depth migration using one-way equations consists of two steps, wavefield extrapolation and imaging.

Wavefield extrapolation used in depth-stepping migration is sometimes called downward continuation. In 1D media, downward continuation is performed in the  $f$ - $k$  domain by the phase-shift operator  $\exp(y\Delta z k_z)$  as described in Equation 8. In 3D media, on the other hand, downward continuation can be performed by space-variant convolution in the  $f$ - $x$  domain as described in Equation 9 using the optimized filter coefficients  $W^v(m\Delta x, n\Delta y, \hat{k}_0)$ .

Figure 5 illustrates the depth-stepping using these filter coefficients. The filter coefficients  $W^v(m\Delta x, n\Delta y, \hat{k}_0)$  are functions of the normalized (or dimensionless) wavenumbers as described in the previous section. The filter coefficients are precomputed and accessible via tables, where the respective depth-stepping length  $\Delta z$ , angular frequency  $\omega$  and local conductivity  $\sigma$  (or velocity) determine the correct operator at each grid point during the downward continuation process. Once the filter operators are designed, the resulting wave-propagation algorithm is simple and eminently suited for implementation on large parallel computing systems (Holberg, 1988).

It should be noted that the  $f$ - $k$  and FD depth-migration methods based on one-way equations do not handle wavefield amplitudes accurately. In fact these schemes were never assumed to do so. Hence, the result of depth migration is a relative structural image of the resistivity (or velocity) contrasts. Full inversion must be used to compute estimates of the subsurface parameter model.

*Imaging conditions.* At each depth  $z$  the electric field in spatial coordinates can be obtained by an inverse Fourier transform over horizontal wavenumbers

$$E_j^r(\mathbf{x}) = \frac{1}{(2\pi)^2} \int_{-\infty}^{\infty} \int_{-\infty}^{\infty} dk_x dk_y \exp i(k_x x + k_y y) E_j^r(k_x, k_y, z) \quad (11)$$

Imposing Claerbout's (1985) well-known  $U/D$  imaging condition from seismic migration, the contribution to the image at position  $\mathbf{x} = (x, y, z)$  from angular frequency  $\omega$  is:

$$I(\mathbf{x}, \omega) = \frac{E_j^M(\mathbf{x}, \omega)}{E_j^D(\mathbf{x}, \omega)} = \frac{E_j^M(\mathbf{x}, \omega) E_j^D(\mathbf{x}, \omega)}{|E_j^D(\mathbf{x}, \omega)|^2} \quad (12)$$

**Table 2.** Comparison of important characteristics and requirements for 3D explicit digital filter operator design for seismic data and CSEM.

	Seismic	CSEM
Vertical wavenumber	Discontinuous	Continuous
Wavenumber	Real (propagating) or imaginary (evanescent)	Complex
Dispersion relation	Proportional to frequency	Proportional to square root of frequency
Attenuation/ absorption	Explicit	Implicit
Type of field	Propagation	Diffusion
Optimization	Matching both real and imaginary parts of $k_z$	Matching both real and imaginary parts of $k_z$
Constraint	Magnitude response $\leq 1$	None necessary
Dip limitation	Explicit (e.g., $60^\circ$ )	Implicit

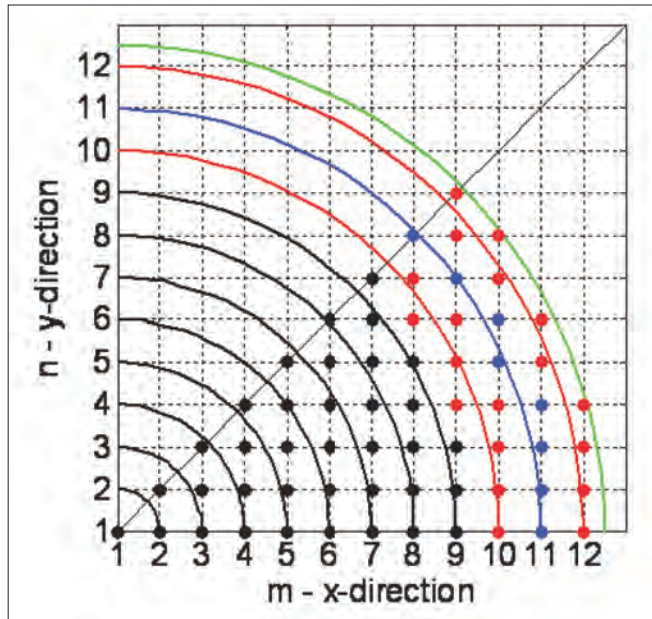


**Figure 2.** Layout of digital filter coefficients. The extrapolation coefficients are shown in the first quadrant only but have symmetric counterparts in the three other quadrants. The core area coefficients are the black circles. The constrained coefficients in the outer area are red and blue circles, alternating with the approximate radius. The arc segments mark the approximate radius. Coefficients with identical symbols along each segment are assumed identical.

The total image is obtained by summing over frequencies

$$I(\mathbf{x}) = \int_{-\Omega}^{+\Omega} d\omega I(\mathbf{x}, \omega) = 2 \int_0^{\Omega} d\omega \operatorname{Re}\{I(\mathbf{x}, \omega)\} \quad (13)$$

where  $\Omega$  is the maximum angular frequency.

The above imaging condition assumes that the scattered field is due to simple reflection phenomena. It is applicable to CSEM data in a single-scattering approximation below the critical angle ( $\leq 10^\circ$ ). Near the critical angle, the EM fields are refracted and assumed to propagate as guided fields through the conductivity anomaly. To account for this, Mittet et al. (2005) proposed an extended nonlocal imaging condition which can be written:

$$I(\mathbf{x}, \omega) = \frac{E_j^M(\mathbf{x}, \omega)}{E_j^D(\mathbf{x}, \omega)} \quad (14)$$

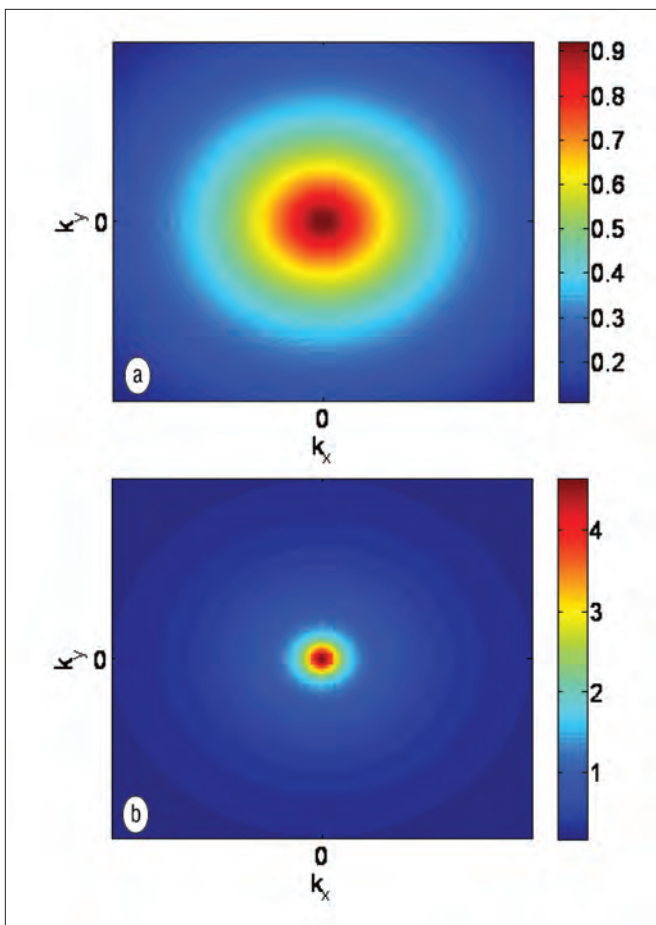


**Figure 3.** The f-k responses of phase-shift operator for downgoing EM wavefields. Magnitude (a) and phase (b) of frequency response of Green's function.

where in principle

$$\hat{E}_j^D(\mathbf{x}, \omega) = \int d^2 \mathbf{x}' h(\mathbf{x}, \mathbf{x}') E_j^D(\mathbf{x}', \omega) \quad (15)$$

The function  $h(\mathbf{x}, \mathbf{x}')$  effectively introduces an extra phase shift in the downgoing field  $\hat{E}_j^D(\mathbf{x}', \omega)$ . The phase shift depends on the local conductivity of the anomaly that we want to image.

**Numerical example.** The described 3D explicit finite-difference depth migration scheme will be tested on field SBL data from Troll Field offshore Norway. This survey was presented in detail by Johansen et al. (2005), and provided irrefutable evidence for direct detection of deeply buried hydrocarbon accumulations by CSEM.

Troll Field's water depth is approximately 325 m, and the reservoir is about 1125 m below the seabed. The thickness of the reservoir is 100–200 m. Resistivity is higher than 100 ohm-m. The SBL survey used 24 EM receivers along a 2D line in the SW–NE direction that crossed the Troll West Gas Province (TWGP). Eighteen receivers were equipped with both electric and magnetic field sensors, and six receivers were equipped only with electric field sensors. The data for the 18 receivers with both electric and magnetic sensors were processed to attenuate the “air wave” in shallow water by a wavefield decomposition technique (Amundsen et al., 2006) and the data will be used in the numerical example. The horizontal electric dipole emitted a continuous square-wave signal at a fundamental frequency

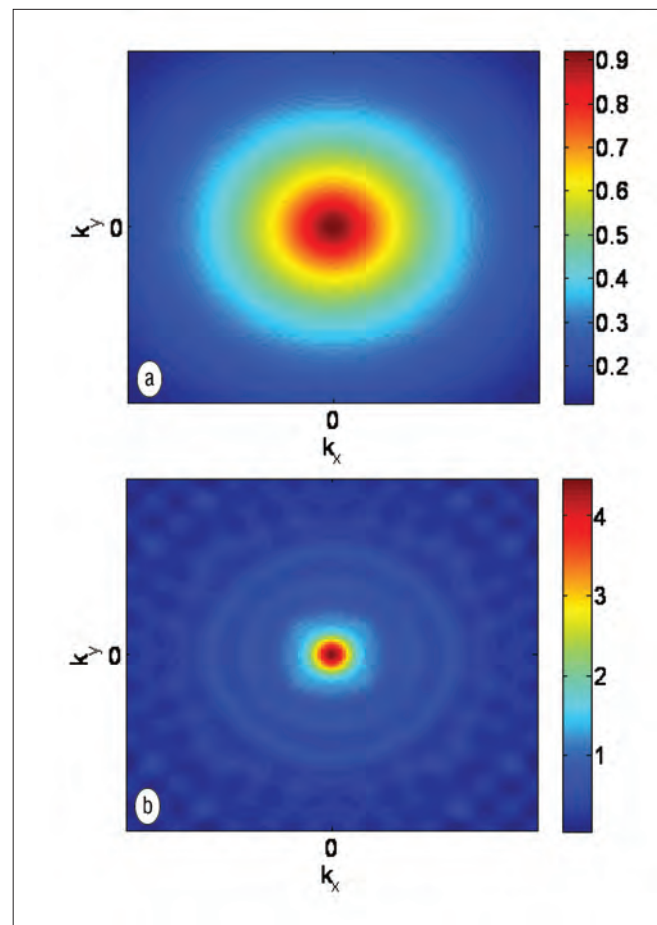


**Figure 4.** The f-k responses of optimized digital filter for downgoing EM wavefields. Magnitude (a) and phase (b) of frequency response of optimized digital filter.

of 0.25 Hz and with a source dipole moment of more than 200 kA.

Data with frequencies 0.25 Hz, 0.75 Hz, and 1.25 Hz are used. The water conductivity is 3.2 S/m, and the horizontal conductivity is  $\sigma = 0.67$  S/m. Figure 6 shows the depth-migrated section. Notice the excellent match of the conductivity anomaly and the TWGP reservoir represented by the black rectangle (approximately 200 m thick). The “hole” that can be indicated in the middle of the imaged anomaly is due to a missing receiver (i.e., an acquisition footprint).

**Conclusion.** This paper has presented some similarities and dissimilarities between depth migration of seismic and CSEM data. Most  $f$ - $x$  migration schemes developed for seismic imaging can easily be adapted for depth migration of CSEM data. Due to much more sparsely sampled data and fewer discrete frequencies, frequency-domain MCSEM depth migration will run about three orders of magnitude faster than seismic data.

**Suggested reading.** “Elimination of free-surface related multiples without need of the source wavelet” by Amundsen (GEOPHYSICS, 2006). “Decomposition of electromagnetic fields into upgoing and downgoing components” by Amundsen et al. (GEOPHYSICS, 2006). “3D table-driven migration” by Blacquiere et al. (*Geophysical Prospecting*, 1989). “Wave equation migration with the phase-shift method” by Gazdag (GEOPHYSICS, 1978). “Anisotropic depth migration of marine controlled-source

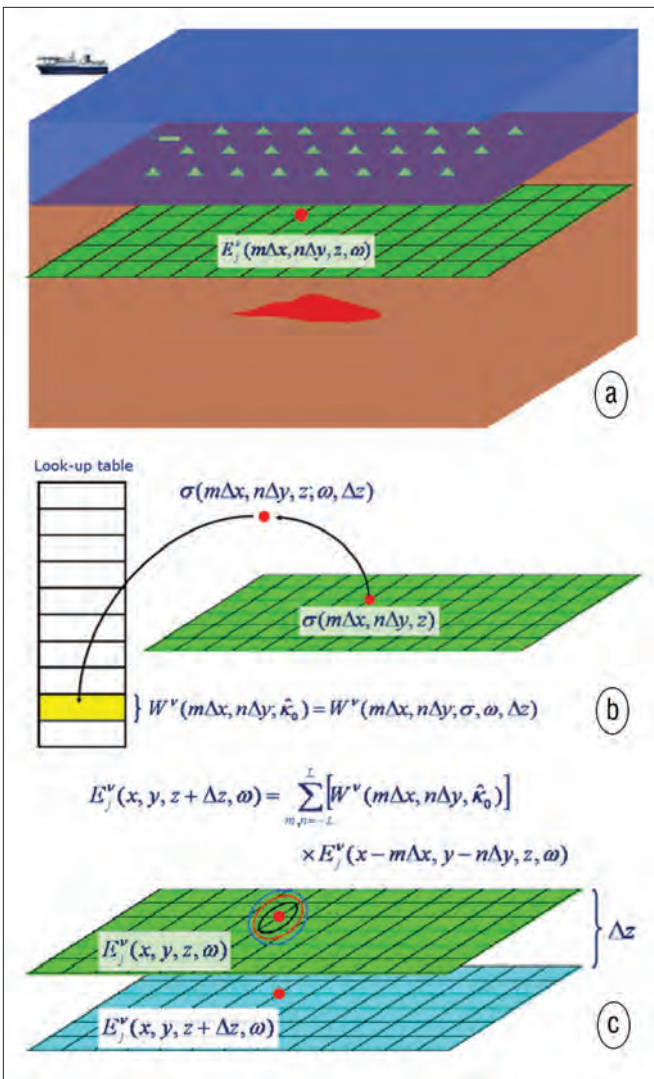


**Figure 5.** Illustration of wavefield extrapolation in the  $f$ - $x$  domain. (a) Electric wavefield component  $E_j^v(m\Delta x, n\Delta y, z)$  at angular frequency  $\omega$ . (b) Accessing the filter lookup table index representing the filter coefficients  $W^v(\Delta x, \Delta y, \kappa_0)$  using the local gridpoint conductivity, given the frequency and depth-stepping length as input,  $\sigma(m\Delta x, M\Delta y, z; \omega, \Delta z)$ . (c) Wavefield extrapolation of the local grid point given in (a) and (b) from  $z$  to  $z + \Delta z$  by discrete convolution according to Equation 9.

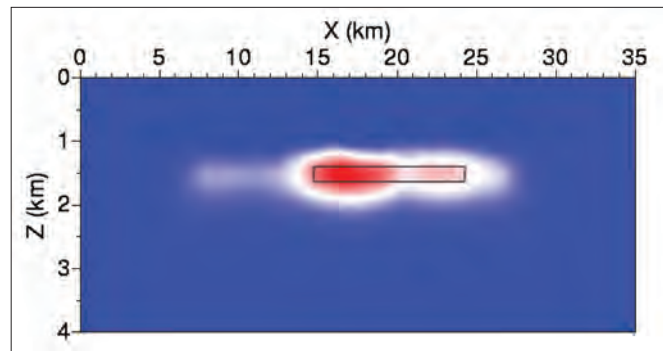


**Figure 6.** 3D explicit finite-difference depth-migration of the SBL data from Troll Field.

electromagnetic data" by Hokstad and Røsten (*EAGE 2006 Extended Abstracts*). "Towards optimum one-way wave propagation" by Holberg (*Geophysical Prospecting*, 1988). "Subsurface hydrocarbons detected by electromagnetic sounding" by Johansen et al. (*First Break*, 2005). "Low-frequency electromagnetic fields in applied geophysics: Waves or diffusion?" by Løseth et al. (*GEOPHYSICS*, 2006). "Prestack depth migration with compensation for absorption and dispersion" by Mittet (*GEOPHYSICS*, 1995). "A two-step approach to depth migration of low-frequency electromagnetic data" by Mittet et al. (*SEG 2005 Expanded Abstracts*). "Explicit 3D depth migration with a constrained operator" by Mittet (*GEOPHYSICS*, 2006). "3D depth migration operators for marine controlled-source electromagnetic data" by Røsten et al. (*SEG 2006 Expanded Abstracts*). "Marine controlled-source electromagnetic imaging for hydrocarbon exploration: interpreting subsurface electrical properties" by Tompkins (*First Break*, 2004). "Underground imaging by frequency-domain electromagnetic migration" by Zhdanov et al. (*GEOPHYSICS*, 2005).

*Acknowledgments:* We thank Statoil ASA for permission to publish this work.

*Corresponding author:* kehok@statoil.com